

FEM-based analysis on sensing out-of-plane displacements of low-order Lamb wave modes by CMUTs

Cite as: J. Appl. Phys. **132**, 204502 (2022); <https://doi.org/10.1063/5.0123393>

Submitted: 30 August 2022 • Accepted: 01 November 2022 • Published Online: 23 November 2022

 Wei Lu,  Sai Zhang,  Renxing Wang, et al.



View Online



Export Citation



CrossMark

ARTICLES YOU MAY BE INTERESTED IN

[Simulating the magnetic fields generated by piezoelectric devices using FEM software: Beyond the quasistatic approximation](#)

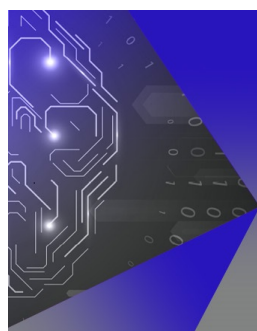
Journal of Applied Physics **132**, 205107 (2022); <https://doi.org/10.1063/5.0120630>

[Describing the dynamics of a nonlinear viscoelastic shelled microbubble with an interface energy model](#)

Journal of Applied Physics **132**, 204702 (2022); <https://doi.org/10.1063/5.0127399>

[Electromagnetic analogs of quantum mechanical tunneling](#)

Journal of Applied Physics **132**, 200901 (2022); <https://doi.org/10.1063/5.0118308>



APL Machine Learning

Machine Learning for Applied Physics
Applied Physics for Machine Learning

**First Articles
Now Online!**

FEM-based analysis on sensing out-of-plane displacements of low-order Lamb wave modes by CMUTs

Cite as: J. Appl. Phys. 132, 204502 (2022); doi: 10.1063/5.0123393

Submitted: 30 August 2022 · Accepted: 1 November 2022 ·

Published Online: 23 November 2022



Wei Lu,¹ Sai Zhang,^{1,2,a)} Renxing Wang,² Yuhua Yang,² Guojun Zhang,² Wendong Zhang,²
Baiqiang Xu,¹ and Mehmet Yilmaz^{3,4}

AFFILIATIONS

¹Institute of Ultrasonic Testing, Jiangsu University, Zhenjiang 212013, China

²State Key Laboratory of Dynamic Testing Technology, North University of China, Taiyuan 030051, China

³Institute of Materials Science and Nanotechnology, Bilkent University, Ankara 06800, Turkey

⁴UNAM—National Nanotechnology Research Center, Bilkent University, Ankara 06800, Turkey

^{a)}Author to whom correspondence should be addressed: zhangsai@ujs.edu.cn

ABSTRACT

It is well known that acoustic emission (AE) signals, generated by external impacts or damages such as crack initiation, mainly propagate in the form of Lamb waves in plate-like structures. In this work, MEMS-based resonant capacitive micro-machined ultrasonic transducers (CMUTs), which are designed for sensing out-of-plane displacements, have been verified by finite element method (FEM) modeling and theoretical analysis for their feasibility of detecting low-order Lamb waves (A₀ and S₀). First, combining the propagation theory of Lamb waves and the “spring-mass-damper” model of CMUTs, the out-of-plane sensing mechanism has been explained, together with the analytical expression of sensitivity. Then, simulations based on FEM have been carried out to show that the designed CMUTs are sensitive to out-of-plane displacements, while extremely insensitive to in-plane displacements. Meanwhile, a transient analysis has found the potential abilities of CMUTs for sensing A₀ and S₀ lamb waves. Besides, the sensing characteristics of CMUTs have also been investigated, including the influence of squeezed-film damping, the amplitude of the input signal, the cell number, and cell space. Finally, the ball drop impact is simulated to show the potential of identifying the location of the AE source by CMUTs. Our studies reveal the out-of-plane sensing behaviors of CMUTs for Lamb waves and may have the potential in promoting the miniaturization and integration of AE sensors.

Published under an exclusive license by AIP Publishing. <https://doi.org/10.1063/5.0123393>

I. INTRODUCTION

In the past two decades, capacitive micro-machined ultrasonic transducers (CMUTs), which are considered as the most promising alternatives to traditional piezoelectric transducers,^{1,2} have been greatly developed in the medical field for applications such as medical ultrasound imaging,^{3–6} high-intensity focused ultrasound (HIFU) for tumor treatment,^{7,8} and intravascular ultrasound.⁹ In view of the successful cases of CMUTs in medical applications, many scholars started to seek applications of CMUTs in the field of structural health monitoring (SHM).^{10–16}

The acoustic emission (AE) technique, known as the SHM method of capturing and processing the stress-wave signals (usually between 100 kHz and 1 MHz¹⁰) rapidly released during the

development of structural damages, e.g., cracks,¹⁷ delamination,¹⁸ and fatigue,¹⁹ could diagnose the damage status of structures in service. Transducers are one of the key components of data acquisition in AE systems. Usually, it is desirable that the transducers have high sensitivities in a broad frequency range of interest. Currently, piezoelectric transducers, as the widely applied transducers in SHM, can be designed to be resonant or broadband,²⁰ so as to detect signals in the needed frequency range. Although piezoelectric transducers have many merits, e.g., high sensitivity, high signal-to-noise ratio, and wideband, there are still many limitations, e.g., expensive manufacturing costs, significant temperature-influenced performance, and centimeter-scaled sizes.

The emergence of CMUTs makes it possible to solve these limitations. Based on the techniques of the micro-electro-mechanical

system (MEMS), the constituted cells of a CMUT can be designed and fabricated on the micrometer scale with high integration capability,¹⁰ so that they can be embedded in small structures/devices for real-time damage detections, which is difficult to be realized by piezoelectric cells. Besides, as confirmed in previous works, 3D information of particle displacements is much meaningful for accurate damage imaging and evaluation.^{21,22} Benefiting from the advantage of sizes, it is pointed out that 3D sensing of particle displacements may be realized by collocating two CMUTs sensitive to in-plane displacements and one CMUT sensitive to out-of-plane displacements together.²³ Although CMUTs do not perform as good as piezoelectric transducers in terms of sensitivity and signal-to-noise ratio, it is believed that significant performance improvements will be achieved with more research to mature the CMUT technology.

Up to now, many verification studies have been carried out to show the feasibility of applying CMUTs in SHM.^{10–16,24,25} For instance, Ozevin *et al.*¹⁰ demonstrated the possibility of using CMUTs by simulating AE events on a pre-cracked rectangular steel beam specimen. Hossain Saboonchi *et al.*¹³ used the MetalMUMPs technique to design and realize CMUTs with high aspect ratio geometry, the sensitivities of which are comparable to the piezoelectric ones. The ball drop impact and the pencil lead break tests are studied to show their abilities to collect AE signals on an aluminum plate with a thickness of 1 mm. Hossain Saboonchi *et al.*¹⁵ studied CMUTs on damage detection of aluminum 7075 specimens. It was found that CMUTs not only behave similar to piezoelectric transducers from the aspect of crack detection, but also have the advantage of perceiving the initiation and growth of fatigue cracks due to their lower threshold level. Minoob Kabir *et al.*¹⁴ designed, characterized, and compared the in-plane-sensed interdigital CMUTs with area changes and gap changes from the aspects of theory and simulation. Experimental results about detecting the initiation and growth of fatigue cracks on a notched beam-like aluminum coupon have shown their in-plane sensing behaviors. Redha Boubenia *et al.*^{24,25} designed and fabricated a CMUT transducer using the micro-machined MUMPs technique and then demonstrated its ability to detect AE events on an aluminum plate-like structure by comparing with piezoelectric transducers.

It is known that plate-like structures widely exist in major facilities, e.g., aircrafts, high-speed rails, and ships. The AE signals in the plate-like structures propagate almost in the form of Lamb waves, whose characteristics of being multi-mode (i.e., signals may be constituted of multiple propagation modes) and dispersive (i.e., the wave velocity is different for different frequencies) would increase the difficulties of analyzing and processing signals.²⁶ Previous studies mainly focused on the experimental verification of detecting AE events by CMUTs; however, there were no thorough theoretical and simulated analysis on the characteristics of the output signals. Therefore, the sensing performance and the output characteristics of CMUTs for sensing Lamb waves have been analyzed from the aspects of theory and finite element method (FEM) simulation in this work.

Our work is focused on CMUTs that are sensitive to out-of-plane displacements. The article is arranged as follows: In Sec. II, the mechanism of sensing the out-of-plane displacements of Lamb waves using CMUTs has been revealed by combining the propagation theory of Lamb waves and the vibration theory of the

“spring-mass-damper” system; In Sec. III, FEM simulations are carried out to sense the low-order A0 and S0 lamb waves using CMUTs. Besides, the sensing characteristics of CMUTs have been investigated, including directional sensitivity and the influence of squeezed-film damping, the amplitude of the input signal, the number of cells, and cell spacing; In Sec. IV, the ball drop impact is simulated to verify the possibility of locating the AE source by using CMUTs. In Sec. V, relevant results are summarized, and the prospects for future research are given.

II. THEORETICAL MODELING OF A RESONANT CMUT FOR SENSING OUT-OF-PLANE DISPLACEMENTS OF LAMB WAVES

A. The fundamental theory of Lamb waves in a plate

The problem of Lamb waves propagating in an isotropic plate with a thickness of d can be seen as the three-dimensional model shown in Fig. 1(a), with the whole structure extending infinitely along the x axis and the y axis. At top ($z = d/2$) and bottom ($z = -d/2$) surfaces, the “traction-free boundary condition” should be satisfied for the propagation of Lamb waves. According to the wave structure across the thickness of the plate, Lamb waves can be divided into two different propagation modes, i.e., the symmetric modes (S) and the asymmetric modes (A), of which phase velocity dispersion relations are given by the classical Rayleigh–Lamb frequency equations,²⁷

$$\frac{\tan(qd/2)}{\tan(pd/2)} = -\frac{4k^2pq}{(q^2 - k^2)^2} \quad \text{for symmetric modes,} \quad (1)$$

$$\frac{\tan(qd/2)}{\tan(pd/2)} = -\frac{(q^2 - k^2)^2}{4k^2pq} \quad \text{for asymmetric modes,} \quad (2)$$

where

$$p = \sqrt{\frac{\omega^2}{c_t^2} - k^2},$$

$$q = \sqrt{\frac{\omega^2}{c_l^2} - k^2},$$

$$k = \frac{\omega}{c_p},$$

with ω , c_t , c_l , and c_p representing the angular frequency, solid longitudinal wave velocity, solid transversal wave velocity, and Lamb waves' phase velocity, respectively. Solving Eqs. (1) and (2), we can receive the dispersion relations of a traction-free aluminum plate, as shown in Fig. 1(b) (here, thickness $d = 3$ mm). For a specific frequency, at least two low-order propagation modes (i.e., A0 and S0) can exist in a plate at the same time. Besides, with the increase in frequency, more propagation modes would appear (e.g., A1, S1, A2, S2, etc.). For the AE signals in a thin plate-like structure, the

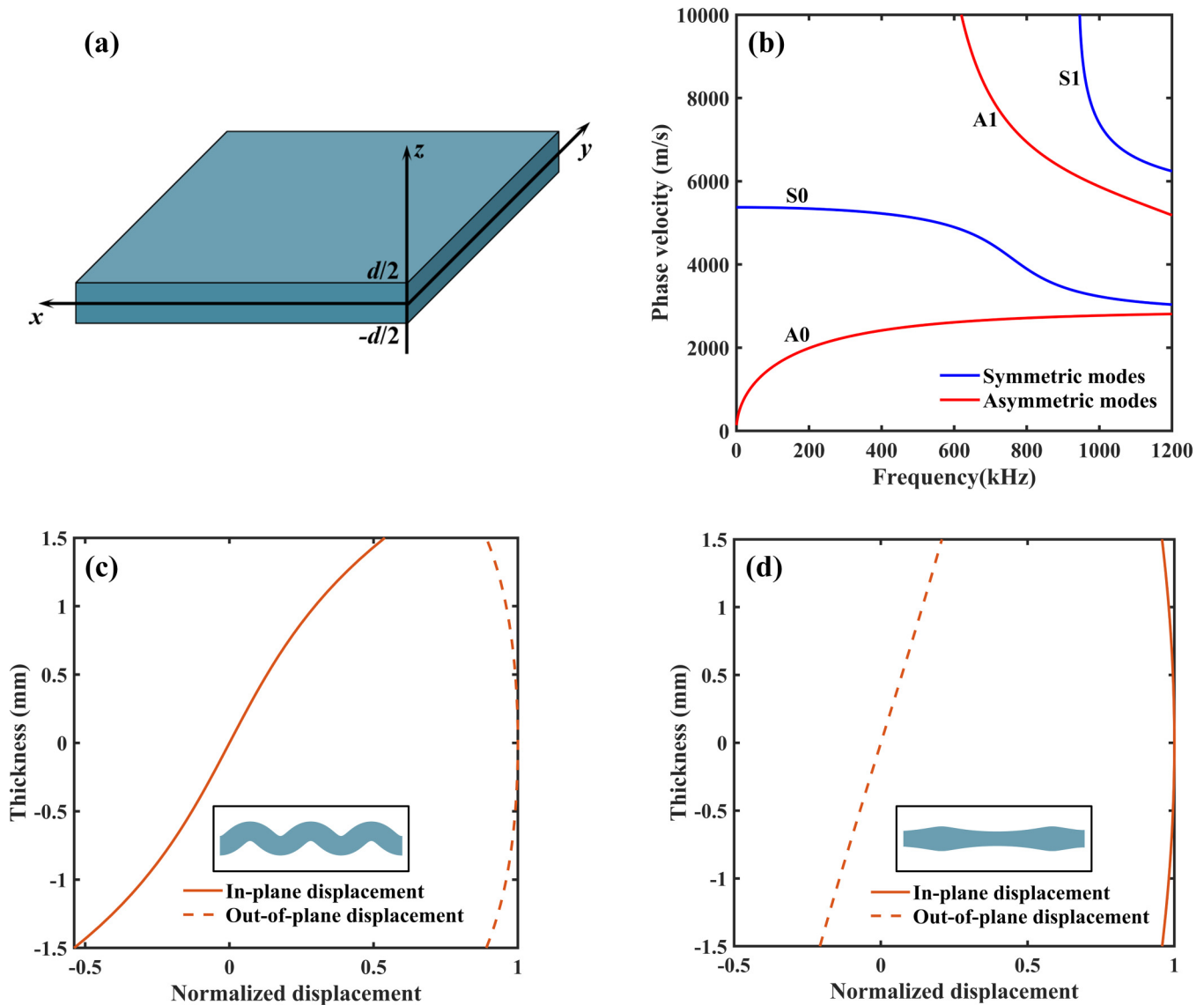


FIG. 1. (a) Three-dimensional diagram of the plate with a thickness of d , where the plane $z = d/2$ and $z = -d/2$ are top and bottom surfaces, respectively; (b) phase velocity dispersion curves of a traction-free aluminum plate with $d = 3$ mm; wave structures of Lamb waves at 220 kHz: (c) A0 mode; (d) S0 mode, where the embedded figures show corresponding deformations along the z - x or z - y plane.

low-order A0 and S0 lamb waves are dominant. Thus, only the low-order A0 and S0 lamb waves are considered in this study.

The in-plane displacements (u) and the out-of-plane displacements (w) across the direction of thickness satisfy the following equations:²⁷

$$u = ikA_2 \cos(pz) + qB_1 \cos(qz), \tag{3}$$

$$w = -pA_2 \sin(pz) - ikB_1 \sin(qz) \tag{4}$$

for symmetric modes and

$$u = ikA_1 \sin(pz) - qB_2 \sin(qz), \tag{5}$$

$$w = pA_1 \cos(pz) - ikB_2 \cos(qz) \tag{6}$$

for asymmetric modes, where A_1 , A_2 , B_1 , and B_2 can be determined by the traction-free boundary condition.²⁷ For instance, the wave structures of Lamb waves in a traction-free aluminum plate with

$d = 3 \text{ mm}$ are given in Fig. 1(c) (A0 mode with 220 kHz) and Fig. 1(d) (S0 mode with 220 kHz). For the A0 lamb waves, the wave structure across the thickness of the plate is anti-symmetric for the in-plane displacement and symmetric for the out-of-plane displacement (the out-of-plane displacement is dominated at low frequencies). Conversely, the wave structure of the S0 lamb waves across the thickness is symmetric for the in-plane displacement and anti-symmetric for the out-of-plane displacement (the in-plane displacement is dominated at low frequencies).²⁷

B. Theory of sensing out-of-plane displacements of Lamb waves by a resonant CMUT

Figure 2 shows the structural design and the detection principles of a resonant CMUT cell, which is designed to be sensitive to out-of-plane displacements. As reported in Ref. 13, the resonant CMUT cell may be composed of an electroplated layer (Au, height d_{Au}), a top electrode (polycrystalline silicon, height d_{top}), gap (air, height d_{gap}), an insulation layer (Si_3N_4 , height $d_{\text{Si}_3\text{N}_4}$), a bottom electrode (polycrystalline silicon, height d_{bottom}), springs (height $d_{Au} + d_{top}$), and anchors [Fig. 2(a)], where the electroplated layer is used for wiring, the insulation layer is introduced for preventing electrical short circuits, and the L-shaped springs and the

anchors serve to suspend the top electrode. The lengths of each layer along the x axis and the y axis are set as l . The L-shaped springs are divided into two sections with the widths being w , where the first section (see Fig. 2, Spring 1) has the length of l_1 and the second section (see Fig. 2, Spring 2) has the length of $l_2 - w$. The distances between the springs and edges are set as d . In order to sense waves with different frequencies, the shape and the length of springs should be adjusted to achieve the required resonant frequency. In the micrometer scale, squeezed-film damping caused by the compression of air in the gap cannot be ignored. The squeezed-film damping behavior would decrease the sensitivity of CMUT significantly.²⁸ There are at least two ways to reduce the squeezed-film damping, i.e., vacuuming and sealing the capacitive gap [Fig. 2(a)] or etching periodic through holes in the vibrating top electrode¹³ [Fig. 2(b)]. The lengths of through holes along the x axis and the y axis are labeled as a_n and b_n , respectively. From the perspective of technology, these CMUT cells could be manufactured by the PolyMUMPs process.¹³

The simplified “spring-mass-damper” system can be used to predict the working behavior of a CMUT cell²⁹ at low frequencies, as shown in Fig. 2(c). The electroplated layer and the top electrode together constitute the mass m . The L-shaped springs can be assumed as an equivalent spring with the spring constant of k .

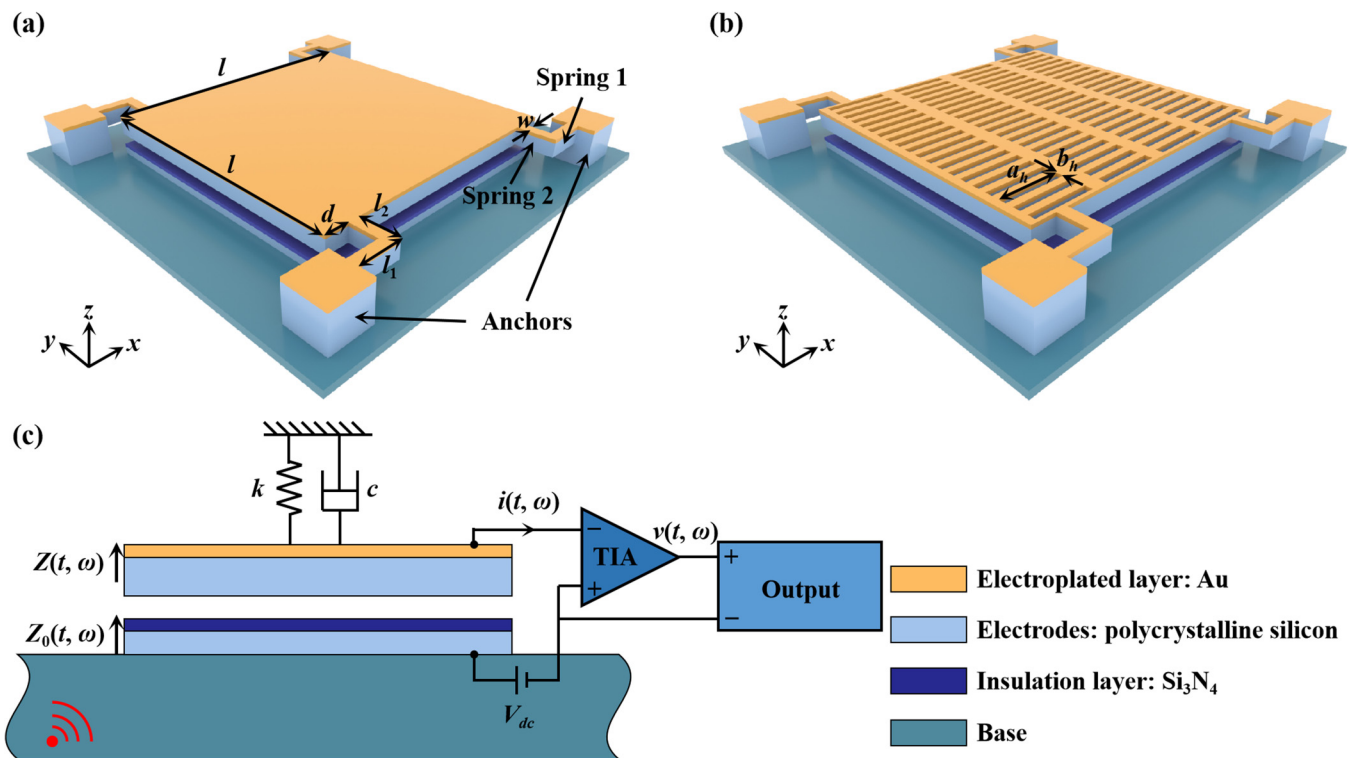


FIG. 2. Diagrams of the resonant CMUT cells that are sensitive to out-of-plane displacements: (a) with no etching holes; (b) with periodic etching holes to reduce the squeezed-film damping.¹³ (c) shows the working principles of the CMUT cell for AE detection. The red-colored symbol at the left bottom of the figure represents the AE source. A transimpedance amplifier (TIA) is employed to convert the current into a voltage output.

The bottom electrode is directly in contact with the surface of the base. The relative movement between the mass and the bottom electrode is assumed as that of a piston.

Assume that Lamb waves are released from the AE events of a plate. The out-of-plane displacements of Lamb waves at the surfaces of the plate ($z = \pm d/2$) would couple into the bottom electrode and then lead to the out-of-plane displacement responses of Z_0 (the bottom electrode) and Z (the top electrode relative to the bottom electrode). The motion equation should have the form as

$$m\ddot{Z} + c\dot{Z} + kZ = -m\ddot{Z}_0, \tag{7}$$

where m , c , and k represent the mass, viscous damping constant, and spring constant, respectively.

Assume that the input out-of-plane displacement is a harmonic function of time, t , and frequency, ω ,

$$Z_0(t, \omega) = Awe^{i\omega t}, \tag{8}$$

where the coefficient A is the amplitude and w is the out-of-plane displacement of Lamb waves.

By solving Eq. (7) (the detailed derivation is given in the Appendix), Z can be expressed as

$$Z(t, \omega) = \frac{Q\omega^2}{Q(\omega_0^2 - \omega^2) + i\omega\omega_0} Z_0(t, \omega), \tag{9}$$

where $Q = m\omega_0/c$ and $\omega_0 = \sqrt{k/m}$ are the quality factor and the resonant angular frequency of the CMUT cell, respectively.

The CMUT cell can be considered as a parallel plate capacitor,²⁹ with the capacitance under the steady state described as (see details in the Appendix)

$$C = \frac{\epsilon_0 S}{a - d_0}, \tag{10}$$

where

$$a = \frac{d_{Si_3N_4}}{\epsilon_{Si_3N_4}} + d_{gap},$$

$$d_0 = \frac{V_{dc}^2 \epsilon_0 S a}{2(ka^3 - V_{dc}^2 \epsilon_0 S)}.$$

In Eq. (10), S is the facing area between electrodes, V_{dc} is the DC-biased voltage applied on the electrodes, ϵ_0 is the dielectric constant of vacuum, and $\epsilon_{Si_3N_4}$ is the relative permittivity of Si_3N_4 . Besides, a is the effective gap height without the DC-biased voltage, and d_0 is the reduced distance between electrodes under the DC-biased voltage.

Considering the distance between electrodes is dynamic under input out-of-plane displacements, the dynamic capacitance of a

CMUT cell should be expressed as

$$C(t, \omega) = \frac{\epsilon_0 S}{a - d_0 + Z(t, \omega)}. \tag{11}$$

Using Taylor series expansion, Eq. (11) can be approximated by ignoring the high-order terms,

$$C(t, \omega) \approx \epsilon_0 S \left(\frac{1}{a - d_0} - \frac{Z(t, \omega)}{(a - d_0)^2} \right). \tag{12}$$

Correspondingly, the output current of a CMUT cell is a function of the DC bias voltage and the capacitance,²⁹

$$i(t, \omega) = V_{dc} \frac{dC(t, \omega)}{dt}. \tag{13}$$

Substituting Eq. (12) into Eq. (13), the output current of a CMUT cell can be formed as

$$i(t, \omega) = - \frac{i\epsilon_0 V_{dc} S Q \omega^3}{(a - d_0)^2 [Q(\omega_0^2 - \omega^2) + i\omega\omega_0]} Z_0(t, \omega). \tag{14}$$

Usually, a transimpedance amplifier (TIA) and a voltage amplifier are used to convert the current into an output voltage³⁰ and amplify the output voltage, respectively,

$$v(t, \omega) = RUi(t, \omega), \tag{15}$$

where R is the conversion coefficient of the TIA in Ω and U is the amplified coefficient of the voltage amplifier in V/V .

For a resonant CMUT composed of N parallel identical cells, the total output current is the sum of the current of each cell. Traditionally, the sensitivity $H(\omega)$ of a resonant CMUT is defined as the ratio of the output voltage to the input speed. When the total size of CMUT is much smaller than the input wavelength, the input out-of-plane displacement of each constituted cell can be considered as identical due to the nearly identical phase. Thus, $H(\omega)$ has the expression as follows:

$$H(\omega) = 20\log_{10} abs \left(\frac{Nv(t, \omega)}{\dot{Z}_0(t, \omega)} \right)$$

$$= 20\log_{10} abs \left(- \frac{iNRU\epsilon_0 V_{dc} S Q \omega^3}{i\omega(a - d_0)^2 [Q(\omega_0^2 - \omega^2) + i\omega\omega_0]} \right). \tag{16}$$

Based on Eq. (16), the sensitivity of a resonant CMUT, which is used for sensing out-of-plane displacements, can be predicted analytically. However, Lamb waves may not only have the out-of-plane displacements, but also in-plane displacements. Specifically for S0 lamb waves, the in-plane displacements are dominant at low frequencies. It may be much more complicated to consider whether in-plane displacements would influence the out-of-plane sensing performance of a resonant CMUT through theories. Therefore, a numerical method, i.e., FEM simulation, is considered to evaluate the influence, as shown in Sec. III.

III. SIMULATION ANALYSIS ON SENSING THE OUT-OF-PLANE DISPLACEMENTS OF LAMB WAVES BY A RESONANT CMUT

A. Establishment of the 3D simulation model

In this work, the commercial FEM software named COMSOL Multiphysics is used to establish the model of sensing Lamb waves by a resonant CMUT, as schematically shown in Fig. 3. For a resonant CMUT cell [Fig. 3(a)], the simulation model is established by the “electromechanics physics (*emi*)” module and the “laminar flow physics (*spf*)” module as defined in COMSOL, where the *emi* module is constituted of the “solid mechanics physics (*solid*)” module and the “electrostatics physics (*es*)” module. To simulate the compression of air in microstructural geometries, a cubic air domain containing the CMUT cell, which is not shown here for the aim of observing the internal structure, needs to be established in the “laminar flow physics (*spf*)” module. Due to the movement of the top electrode, the boundaries of the air domain in the CMUT cell are variable; thus, the “moving mesh” module should be adopted for the air. To calculate the deformation of the CMUT cell under electrostatic forces, the whole structure should be set as “electrostatics physics (*es*),” while the solid domain as “solid mechanics physics (*solid*).” In the “electrostatics physics (*es*)” module, both top and bottom electrodes are considered as terminals, where the top electrode is applied a DC-biased voltage and the bottom electrode is grounded. The interfaces between “solid mechanics physics (*solid*)” and “laminar flow physics (*spf*)” are fully coupled fluid-structure interaction boundaries, which are used to analyze the squeezed-film damping. Besides, the “electrical circuit physics (*cir*)” module should be used to couple with the “electrostatics physics (*es*)” module for calculating the total output current of a CMUT constituted of multiple parallel cells.

For sensing the Lamb waves, the resonant CMUT is attached to the surface of a plate, as shown in Fig. 3(b). Two point sources (only one of them is visible), which are symmetrically positioned on both sides of the plate, are located at the center of the plate to

generate Lamb waves. To avoid the influence of reflected waves, Rayleigh damping regions are constructed around the plate, which are labeled as dark gray areas. Based on previous simulation experience, the maximum size of the mesh should not be larger than one-sixth of the minimum wavelength for the aim of analyzing Lamb waves accurately. In the transient study, the time step performed by the solver should be set at least $1/(60 \times f_{\max})$, where f_{\max} is the maximum frequency that needs to be solved.

B. Cell design and sensitivity analysis

In order to design an out-of-plane-sensitive CMUT cell that resonates at a specific frequency, first, the eigenfrequency study should be considered. In the eigenfrequency study, the FEM model of a CMUT cell is established as the one that is shown in Fig. 3(a) (squeezed-film damping is not considered in this study), with the bottom surfaces set as fixed boundaries. The adopted material parameters are given in Table I. On this basis, three CMUT cells that are sensitive to three different frequencies (200 kHz for CMUT I, 220 kHz for CMUT II, and 240 kHz for CMUT III) have been designed, of which the cell parameters are shown in Table II.

Figure 4 gives the first three mode shapes that would cause a change in capacitance for each designed CMUT cell. For the first mode shape [see Fig. 4(a) for CMUT I, Fig. 4(d) for CMUT II, and Fig. 4(g) for CMUT III], the top electrode vibrates back and forth along the out-of-plane direction (z axis). The first mode shape is the working mode of each CMUT cell, for sensing out-of-plane displacements. For the second mode shape [see Fig. 4(b) for CMUT I, Fig. 4(e) for CMUT II, and Fig. 4(h) for CMUT III] and the third mode shape [see Fig. 4(c) for CMUT I, Fig. 4(f) for CMUT II, and Fig. 4(i) for CMUT III], the top electrode almost vibrates along the in-plane direction (y axis for the second mode and x axis for the third mode). The in-plane motion of the top electrode relative to the bottom electrode would lead to the change of S , thus resulting in the change of capacitance. However, considering that the eigenfrequency of the in-plane mode is far away from that of the

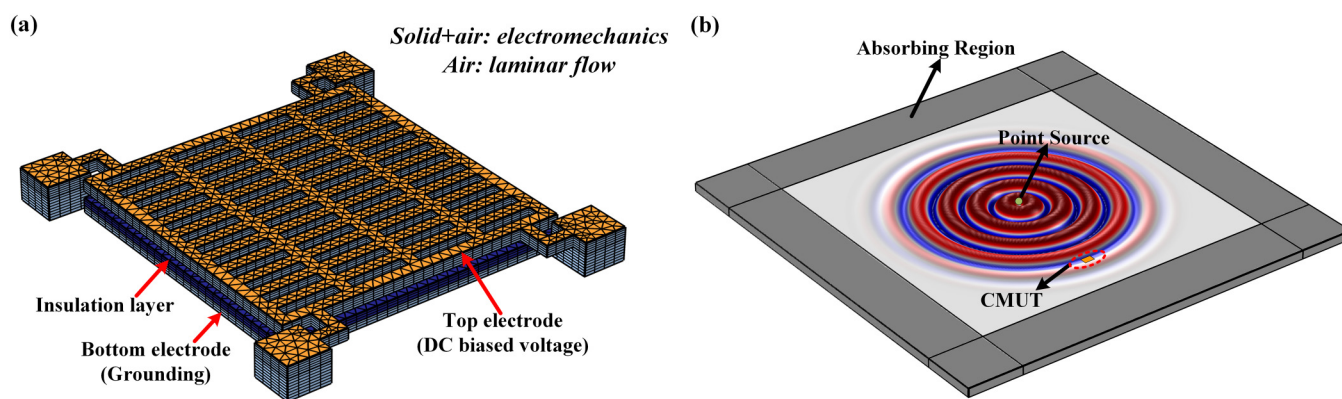


FIG. 3. (a) Established 3D finite element model of a resonant CMUT cell with the mesh included (not drawn to scale). (b) Schematic diagram of sensing the Lamb waves by a resonant CMUT attached to the surface of an isotropic material plate with a traction-free surface. Two point sources (only one of them is visible), which are symmetrically positioned on both sides of the plate, are located at the center of the plate to generate Lamb waves. The dark gray areas around the plate are set as the absorbing region to avoid boundary reflections.

TABLE I. Material parameters used in the simulation.

Solid material				
	Density (kg/m ³)	Young's modulus (GPa)	Poisson's ratio	Relative permittivity
Gold	19 300	70	0.44	
Polycrystalline silicon	2320	160	0.22	4.5
Si ₃ N ₄	3100	250	0.23	9.7
Aluminum	2700	70	0.33	
Fluid material				
	Density (kg/m ³)	Dynamic viscosity (Pa s)	Relative permittivity	
Air	1.21	1.81 × 10 ⁻⁵	1	

out-of-plane mode (e.g., for CMUT I, the first mode is at 200 kHz, while the second mode is at 1.38 MHz), it can be inferred that the in-plane mode may produce little influence on the out-of-plane sensing performance of these designed CMUT cells.

Furthermore, the directional sensitivities (i.e., the sensitivity to the *x*-direction, *y*-direction, and *z*-direction input displacements) of each designed CMUT cell are calculated by the harmonic disturbance study of FEM simulation to verify the inference above. In simulation, squeezed-film damping is assumed as the specific damping ratio of $\xi = 0.04$ (i.e., $Q = 0.5/\xi = 12.5$). The simulated results of directional sensitivities are received from the equation below:

$$H(\omega) = 20\log_{10}abs\left(\frac{RUi(\omega)}{\bar{v}_n(\omega)}\right), n = x, y, \text{ or } z, \quad (17)$$

where $i(\omega)$ is the output current and $\bar{v}_n(\omega)$ is the input average velocity at the bottom electrode (n labels the direction of the velocity).

Both in the theoretical calculation and in the FEM simulation, the number of cells is $N = 1$, the conversion coefficient of TIA is $R = 1000 \Omega$, and the voltage magnification is $U = 100V/V$.

Figure 5(a) shows the way to simulate the directional sensitivities of a CMUT cell. The colorful arrows represent the direction of

input displacements for measuring the sensitivity to this direction. For example, *x*-directional sensitivity of the cell is measured by specifying an *x*-directional displacement to the base (see the green arrow). The calculated directional sensitivities of each CMUT cell are given in Fig. 5(b), where *x*, *y*, and *z* in the parentheses represent the sensitivity to the corresponding input displacements. By observing Fig. 5(b), it is found that each CMUT cell is sensitive to the out-of-plane (*z*-direction) displacements and is extremely insensitive to in-plane (*x*-direction and *y*-direction) displacements. Specifically at the first mode frequencies, the sensitivity of each cell reaches the maximum (about 5.4 dB for CMUT I, 4.7 dB for CMUT II, and 2.7 dB for CMUT III). To investigate the influence of in-plane displacements on the out-of-plane sensing performance of each cell, *x*-directional, *y*-directional, and *z*-directional displacements are simultaneously specified on the base (defined as case 1), where the amplitude of *x*-directional and *y*-directional displacements is set to ten times the *z*-directional displacements. The situation of specifying only out-of-plane displacements on the base is defined as case 2. In theory, the influence of in-plane displacements on out-of-plane sensing results is shown by the difference of output currents. The difference between the output currents of cases 1 and 2 is defined as $\Delta I = |I_1 - I_2|/I_2$, where I_1 is the current for case 1 and I_2 is the current for case 2. The larger the value of ΔI , the greater the influence of in-plane displacements, thus the worse the out-of-plane sensing performance of the cell. Fortunately, since the high-order mode frequencies are far enough from the first mode frequency, the value of ΔI is very small for each cell [see Fig. 5(c)].

TABLE II. Specific parameters of the designed CMUT cells.

	CMUT I	CMUT II	CMUT III
l (μm)	110	100	97
d_{Au} (μm)	0.5	0.5	0.5
d_{top} (μm)	2	2	2
d_{gap} (μm)	1.1	1.1	1.1
$d_{Si_3N_4}$ (μm)	0.35	0.35	0.35
d_{bottom} (μm)	0.7	0.7	0.7
d (μm)	5	10	10
a_h (μm)	22	20	19.4
b_h (μm)	4.4	4	3.88
l_1 (μm)	12.5	17.5	17.5
l_2 (μm)	11	11	11
w (μm)	2.5	2.5	2.5
V_{dc} (V)	24	26.7	24.3
First resonant frequency (kHz)	200	220	240

C. Examples of sensing A0 and S0 lamb waves by resonant CMUT cells

Simulations about sensing A0 and S0 lamb waves by resonant CMUT cells are investigated in this part for further verification of feasibility. As shown in Fig. 3(b), these CMUT cells are attached to the traction-free surface of an aluminum plate (here, $d = 3$ mm) to analyze their transient sensing behaviors. In simulation, a prescribed out-of-plane displacement signal is adopted for *two-point sources* as defined in Sec. III A to generate Lamb waves, where the analytical expression is shown as

$$Z_{input}(t) = B\sin(2\pi f_c t) \left(1 - \cos\frac{2\pi f_c t}{10}\right). \quad (18)$$

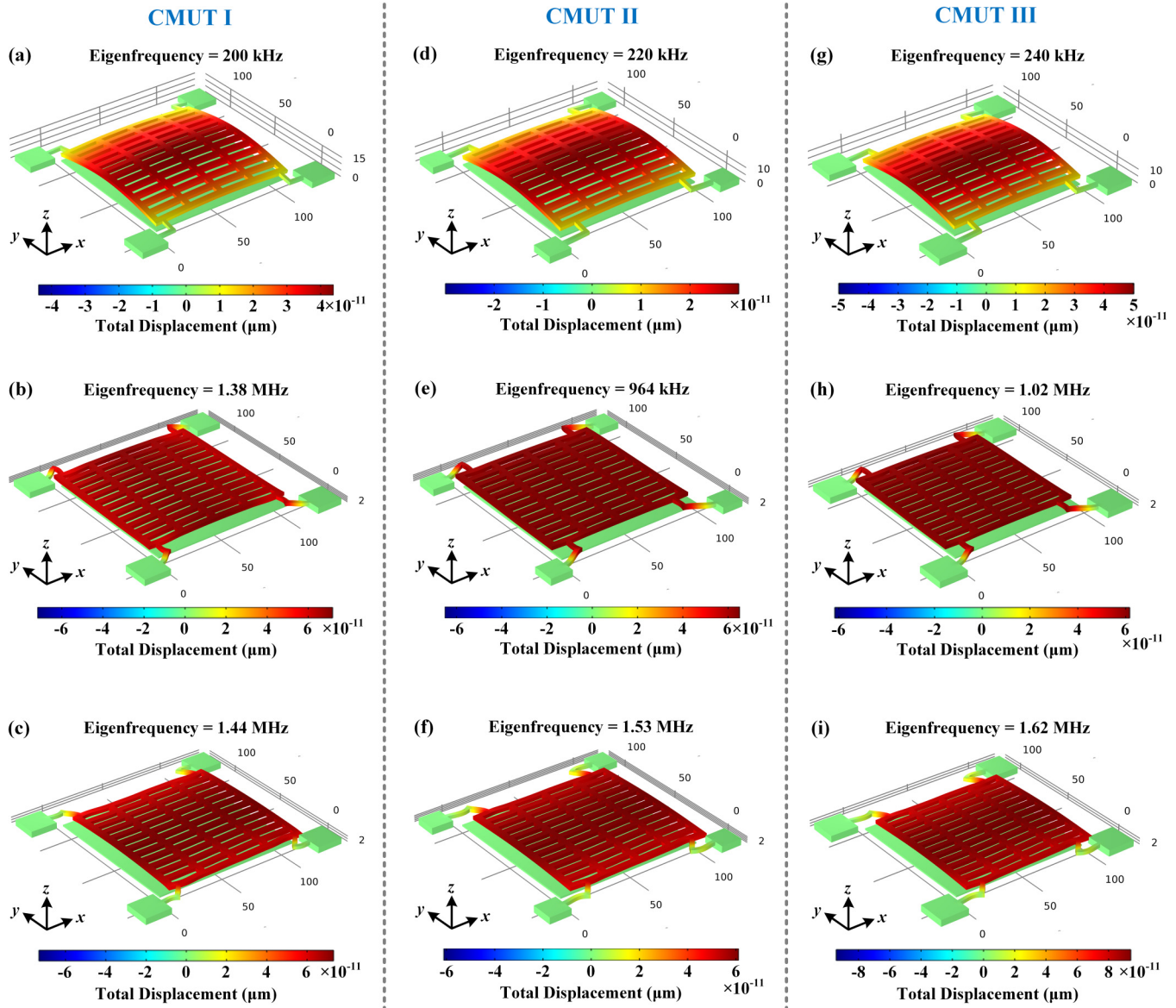


FIG. 4. The first three mode shapes that may cause the change of capacitance of the designed resonant CMUT cell: (a)–(c) are the first three mode shapes of CMUT I; (d)–(f) are the first three mode shapes of CMUT II; and (g)–(i) are the first three mode shapes of CMUT III.

In Eq. (18), f_c is the center frequency and B is the amplitude. The signal is excited at the time of $50/f_c$ (here, 0.227 ms for $f_c = 220$ kHz), with a frequency spectrum covering the sensitive frequencies of each cell. According to the characteristics of the Lamb wave structure, the prescribed out-of-plane displacement of two point sources should be in the same direction to generate A0 mode alone and in the opposite direction to generate S0 mode alone.

Since the value of squeezed-film damping is unknown for each cell, airflow is fully coupled with solid vibration in the simulation to replace the specified damping ratio. Then, the damping

ratio induced by squeezed-film damping can be evaluated by the half-power bandwidth method,¹³

$$\xi = \frac{f_{high} - f_{low}}{2f_{peak}}, \tag{19}$$

where f_{low} and f_{high} are the corresponding lower and higher frequencies when the responses decrease 3 dB from the maximal response and f_{peak} is the frequency corresponding to the maximal

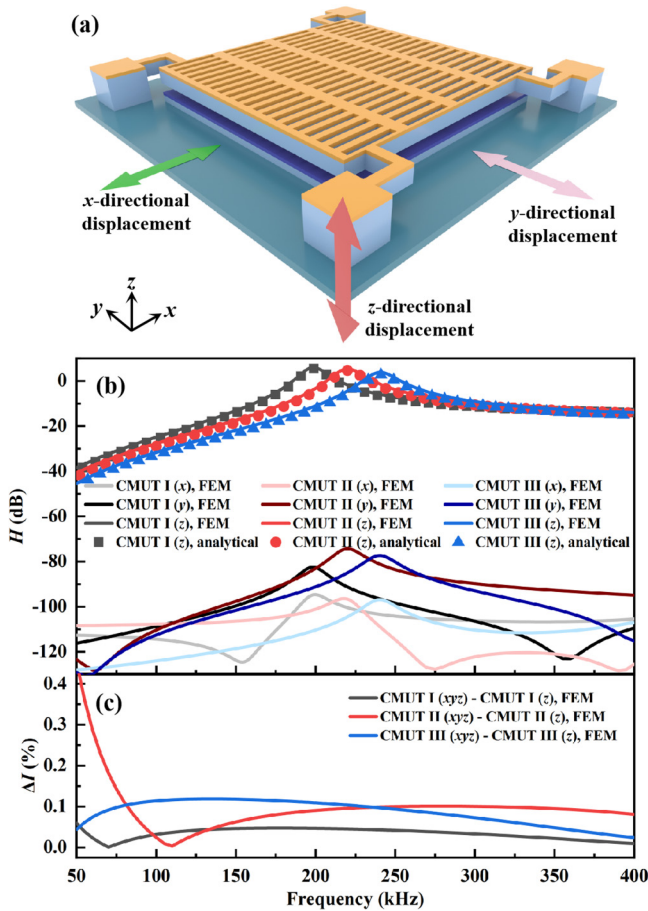


FIG. 5. (a) The way to simulate directional sensitivities (x , y , or z) of a CMUT cell. (b) Directional sensitivity of each designed CMUT cell, where x , y , and z in the parentheses represent the sensitivity to the x -directional, y -directional, and z -directional input displacements, respectively. The FEM results and the analytical results are labeled by colorful solid lines and discrete symbols, respectively. (c) FEM analyzed results of the influence of the in-plane displacements (x and y) on the out-of-plane (z) sensing performance of each cell.

response of the cell. Using fast Fourier transform (FFT) to convert the transient response to frequency-domain first and then using Eq. (19), the damping ratio of each designed CMUT cell can be evaluated. The damping ratio is about 0.032 for CMUT I, 0.028 for CMUT II, and 0.025 for CMUT III.

Figure 6 shows the results of sensing the A0 lamb waves by the designed CMUT cells given in Table II. In the simulation, the amplitude of the prescribed out-of-plane displacement signal is $B = 10$ nm, and the distances between the excited point (impact point) and the CMUT cells are set at 10 mm. The in-plane (u) and the out-of-plane (w) displacement signals arriving to the bottom electrode of the CMUT cells are shown in Fig. 6(a), where the maximal amplitudes are about 1.2 and 2 nm, respectively. The ratio of the out-of-plane displacement to the in-plane displacement is about 1.67, which is consistent with the wave structure of A0 lamb

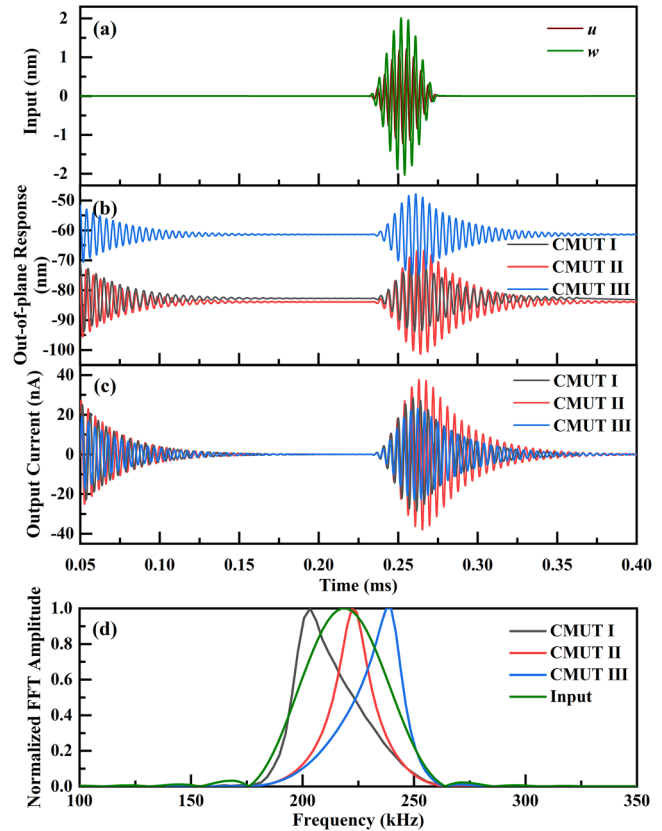


FIG. 6. The results of sensing the A0 lamb waves by the designed CMUT cells: (a) displacements of the arriving signals; (b) the out-of-plane response of each CMUT cell; (c) the output current of each CMUT cell; and (d) FFT results of (a) and (c).

waves shown in Fig. 1(c). The out-of-plane responses of the top electrodes of each CMUT cell are shown after the time of 0.2302 ms, as in Fig. 6(b). The imbalance between the electrostatic force generated by the DC-biased voltage and the elastic restoring force of springs produces a gradually decaying displacement signal before 0.2 ms [this phenomenon can be explained by the general solution to Eq. (9), as shown in the Appendix]. The equilibrium position of the top electrode is about -82.7 nm for CMUT I, -83.9 nm for CMUT II, and -60 nm for CMUT III. Compared with the arriving out-of-plane displacement, w , in Fig. 6(a), the maximal responses are 5.5 times for CMUT I, 9.2 times for CMUT II, and 6.85 times for CMUT III (dividing the maximal out-of-plane response of each cell by the maximal arrived out-of-plane displacement, e.g., $[-82.7 - (-93.83)]/2 \approx 5.5$ for CMUT I). The out-of-plane displacement of the top electrode relative to the bottom electrode leads to the change of capacitance and then produces the corresponding output current [Fig. 6(c)]. Considering the signal of the output current, the propagation velocity of the wave packet is estimated as 3125 m/s (here, propagation distance is 10 mm, excitation starting time is at 0.227 ms, and

arriving time is at 0.2302 ms), which is almost equal to the theoretical group velocity of A0 lamb waves at 220 kHz.²⁷ Therefore, the output signal is determined as A0 lamb waves. Besides, FFT is carried out for the arriving out-of-plane displacement signal [Fig. 6(a)] and the output current signals of each CMUT cell [Fig. 6(c)], as shown in Fig. 6(d). The largest FFT amplitudes of the current signals are about 200, 220, and 240 kHz, which are in agreement with first resonant frequencies of these CMUT cells.

The results of sensing the S0 lamb waves by the designed CMUT cells are shown in Fig. 7. In this case, the amplitude of the prescribed out-of-plane displacement signal is $B = 0.5 \mu\text{m}$, with other settings the same as the A0 case. Different from those of A0 lamb waves, the arrived maximal amplitudes of the in-plane (u) and the out-of-plane (w) displacements at the bottom electrode are about 10 and 2.1 nm, respectively [see Fig. 7(a), u is dominant]. The in-plane displacement is about five times the out-of-plane displacement, which is consistent with the wave structure of S0 lamb waves shown in Fig. 1(d). As shown in Fig. 7(b), the out-of-plane response of the top electrode of each CMUT cell is shown after the time of 0.229 ms, with the amplitude being much larger than

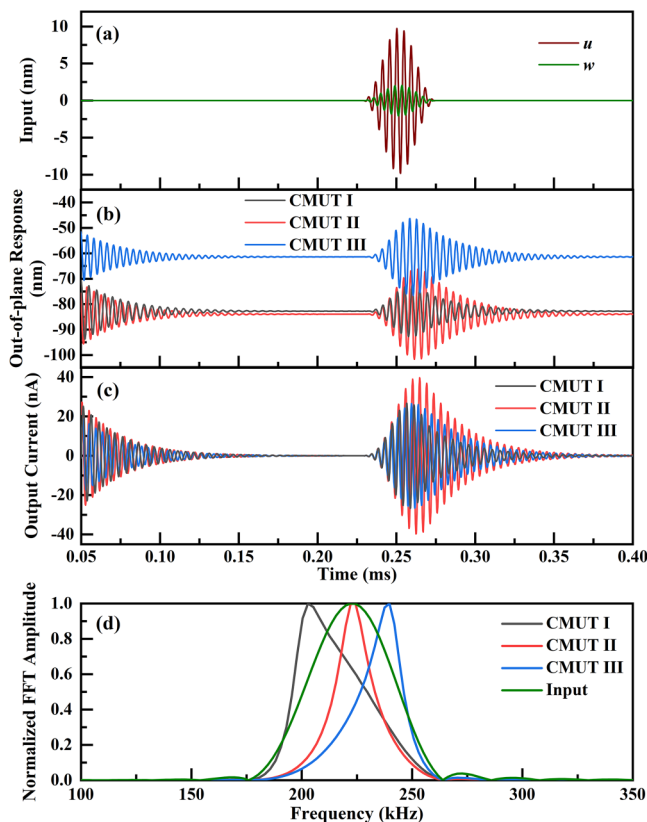


FIG. 7. The results of sensing the S0 lamb waves by the designed CMUT cells: (a) displacements of the arriving signals; (b) the out-of-plane response of each CMUT cell; (c) the output currents of each CMUT cell; and (d) FFT results of (a) and (c).

the arriving one, thus resulting in the corresponding output current [Fig. 7(c)]. Similar to the behavior in Fig. 6(b), the phenomenon of gradually decayed vibration still exists before the time of 0.2 ms. Propagation velocity of the wave packet is also calculated (here, propagation distance is 10 mm, excitation starting time is at 0.227 ms, and arriving time is at 0.229 ms), and the result of which is almost equal to the theoretical group velocity (5254 m/s) of S0 lamb waves at 220 kHz.²⁷ Therefore, the arrived signal is determined as the S0 lamb wave. In this example, FFTs are also carried out for the arrived out-of-plane displacement signal [Fig. 7(a)] and the output currents [Fig. 7(c)], as shown in Fig. 7(d). Due to resonant characteristics of the CMUT cells, the maximal FFT amplitudes of the currents are still at 200, 220, and 240 kHz, respectively.

D. Analysis on the sensing characteristics of a resonant CMUT

The capability of sensing A0 or S0 lamb waves by a resonant CMUT has been confirmed in Sec. III C. In this part, the sensing characteristics of a CMUT cell have been further investigated, including squeezed-film damping, the linearity under a small input signal, the cell number, and cell space.

First, the influence of squeezed-film damping on the output current is studied, as shown in Fig. 8. Three different CMUT cells are designed to receive the out-of-plane signal of Lamb waves on an aluminum plate with thickness $d = 3 \text{ mm}$,

- (i) No through holes are etched on the film ($\gamma = 0\%$, γ is defined as the area ratio of the through holes to the film), and the resonant frequency is $f_0 = 260 \text{ kHz}$;
- (ii) Periodic through holes, with relatively small areas, are etched on the film ($\gamma = 13.8\%$), and the resonant frequency is $f_0 = 245 \text{ kHz}$; and
- (iii) Periodic through holes, with relatively large areas, are etched on the film ($\gamma = 38.4\%$), and the resonant frequency is $f_0 = 220 \text{ kHz}$ (i.e., CMUT II).

The top electrodes of these three CMUT cells are biased to the same displacement position by adjusting the DC-biased voltage, and the other structural parameters are set the same as CMUT II. The excited signal is defined as Eq. (18) with the center frequency of f_c , and the excitation time is at $70/f_c$. By observing Fig. 8, the current signals of these cells are exported at different times, which are determined by frequency f_c and propagation velocities. For the CMUT cell with no through holes [Fig. 8(a)], squeezed-film damping is too large to decrease the output current. With the etching of periodic through holes [Fig. 8(b)], although the electrode area decreases, the release of squeezed-film damping greatly increases the output current (about 14 times). Since the input signal has ten wave peaks [e.g., Fig. 6(a)], the output current should also have ten wave peaks in theory. However, because squeezed-film damping of air is not large enough, the vibration energy of the film cannot be dissipated quickly after the signal input, thus resulting in the phenomenon of tailing [see the blue dotted boxes]. Besides, with the increase in the area of through holes, squeezed-film damping is further released and tailing becomes more serious [Fig. 8(c)]. It should be mentioned that serious tailing would lead

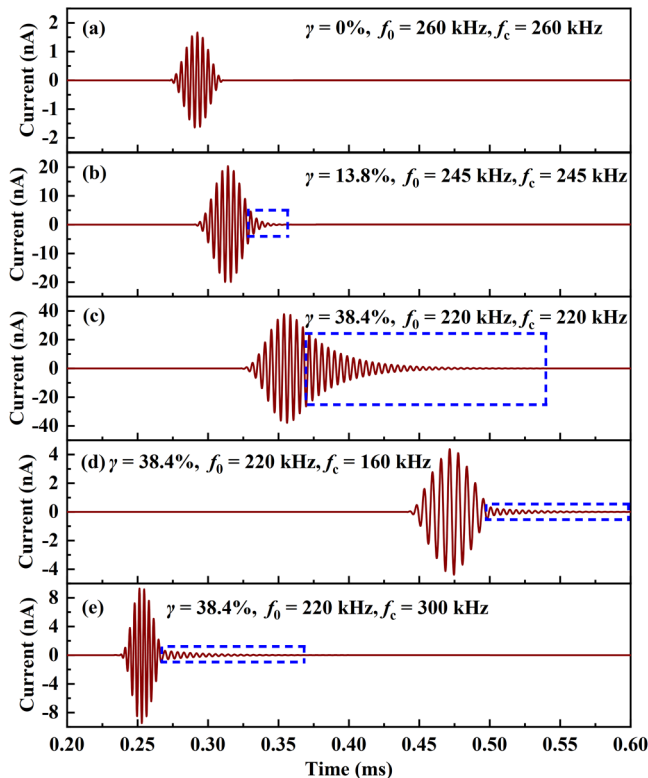


FIG. 8. The output current of CMUT cells with different areas of through holes: (a) $\gamma = 0\%$; (b) $\gamma = 13.8\%$; and (c) $\gamma = 38.4\%$, where the center frequency of the input signal (f_c) is equal to the resonant frequency (f_0) of the cell. (d) and (e) show the output current of the cell, the same as (c), when the center frequency of the input signal (f_c) is far away from the resonant frequency (f_0). Tailings are marked by blue dotted boxes.

to the superposition of signals, which may increase the difficulty of lateral processing.

Furthermore, two different signals with center frequencies (one is 160 kHz and another is 300 kHz) far away from the resonant frequency of 220 kHz are given as input on the cell used in Fig. 8(c) for comparisons. Comparing Fig. 8(c) with Figs. 8(d) and 8(e), it can be observed that sensing signals with center frequencies far away from the resonant frequency of the CMUT cell would significantly reduce the amplitude of the whole output signal (including the tailing); however, it would have little influence on shortening the duration of tailing (see the blue dotted boxes). Differently, releasing squeezed-film damping reasonably could reduce both the amplitude and the duration of tailing significantly [see Figs. 8(b), 8(d), and 8(e)]. Therefore, the output amplitude and tailing should be balanced by adjusting the squeezed-film damping to adapt for sensing the Lamb waves. Besides, it should be mentioned that the maximal amplitude of the output signal for the case of $f_c = 160$ kHz is only about one-tenth of the case of $f_c = 220$ kHz. Considering the low signal-to-noise ratio of CMUTs,²⁹ CMUTs should be used to sense the signal with frequencies around their resonant frequencies.

Then, the output linearity of a CMUT cell under the input out-of-plane displacement is investigated, with the input amplitude increasing from 1 nm to 0.11 μm (see Fig. 9, CMUT II is selected as the research object here). FFT is used to convert the output currents into the frequency domain. It was found that the designed CMUT cell shows perfect linearity under the small input signal (about below 90 nm). However, as the input amplitude increases further (i.e., more than 90 nm), the nonlinearity of CMUT becomes more obvious. The input threshold of CMUT II is about 90 nm. When the input amplitude is higher than the input threshold, nonlinearity would not be ignored. When the input amplitude increases to higher than 110 nm, the moving mesh in the simulation would be so excessively deformed that automatic remeshing is needed to accurately analyze the nonlinearity. However, this automatic remeshing is very time-costly. It should be mentioned that the threshold, which is dependent on the parameters of the designed CMUT cell, is not fixed at 90 nm shown here.

According to the theoretical studies shown in Sec. II B, the total output current of a resonant CMUT should be proportional to the number of constituted cells (N) under the condition that the total size of CMUT is much smaller than the input wavelength. The total output current of a resonant CMUT consisting of multiple identical cells is calculated by transient FEM [here, the CMUT cell is selected the same as that used in Fig. 8(a)] and then transformed into the frequency domain using FFT, as shown in Fig. 10. The distance between cells is set as 150 μm , which is far less than the incident wavelength of A0 lamb waves with a frequency of 260 kHz (about 1/80 of the wavelength). In order to conveniently observe the relationship between the output current and the cell number, the FFT amplitudes are normalized by dividing the FFT

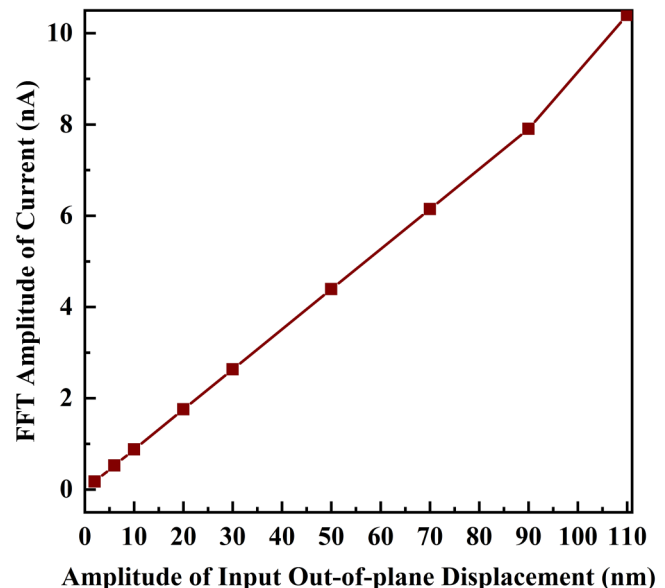


FIG. 9. The linearity of CMUT II under different amplitudes of input out-of-plane displacements.

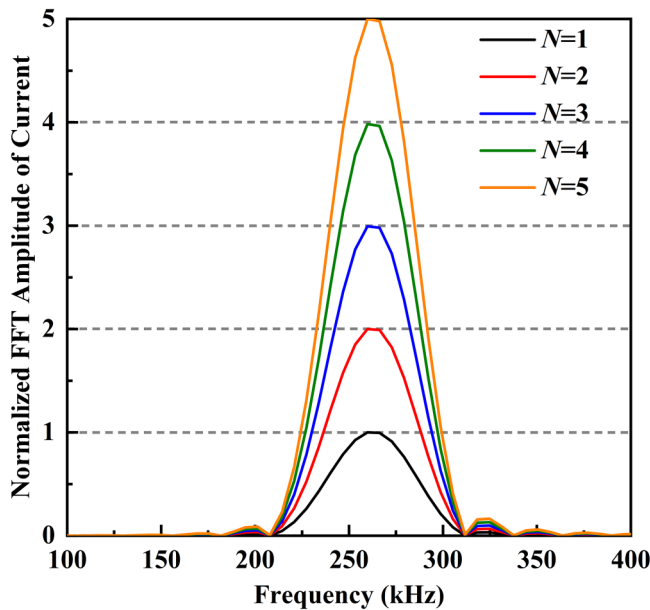


FIG. 10. The influence of the cell number (N) on the FFT amplitude of the output current, where the distance between CMUT cells is $150\ \mu\text{m}$.

peak of a single cell ($N = 1$). With the cell number increasing from $N = 1$ to $N = 5$, the FFT peak of the output current is maintained at 260 kHz, and the magnitudes of these peaks are proportional to the value of N .

The influence of the cell space (D , can be considered as the distance between cells) between CMUT cells on the total output currents is studied in Fig. 11, and the results of which may produce guidance for the design of arrays. Figure 11(a) gives the schematic diagram of the studied array, which is constituted of five identical CMUT cells [here, the cell used in Fig. 8(a) is selected as an example] arranged in a cross-like shape, where the CMUT cells are labeled with numbers from 1 to 5. The cell space between adjacent cells is defined as the distance between cell centers; thus, the span of the array is $2D$. In the study, the value of D is increased from $\lambda/80$ to $\lambda/4$, where λ is the wavelength of A0 lamb waves (for 260 kHz, λ is about 12 mm). Figures 11(b) and 11(c) show the total output currents of the CMUT cells with different cell space and corresponding FFT results, respectively. It was found that with the increase in D , the amplitude of the total output current decreases and reaches the lowest when $D = \lambda/4$ (here, 3 mm). Due to the significant increase in D , the distances away from the excited source are nonignorablely different for each cell, thus resulting in significantly different arriving times of signals [see Fig. 11(d)]. The different arriving time of signals leads to a phase difference between the output currents of each cell and then influences the total output current. In order to illustrate the phase difference more specifically, the out-of-plane displacement distributions of the top electrode of each CMUT cell at 0.1 ms are extracted from the simulation results, as shown in the right figures of Fig. 11(d). For the case of

$D = \lambda/80$ (here, 0.15 mm), the top electrodes of each cell almost move toward the bottom electrodes synchronously [Fig. 11(d)], thus resulting in the maximal total output current [Figs. 11(b) and 11(c)]. For the case of $D = \lambda/4$, the top electrodes of cell 2, cell 3, and cell 4 move toward the bottom electrodes, while those of cell 1 and cell 5 move oppositely [Fig. 11(d)]. The large phase differences between cells make their output currents cancel each other, thus resulting in a lower total current output [Figs. 11(b) and 11(c)]. In the case of $D < \lambda/16$ [the span of the CMUT array ($2D$) is less than $\lambda/8$], the reduction in the total output current is relatively small. Therefore, in order to make full use of the output current of each cell, the array of CMUT cells should be arranged in a dense way, and the overall span of the array should be as less as $\lambda/8$ (here, the value of $2D$ is 1.5 mm and the size of one CMUT cell is only 0.1 mm).

IV. VERIFICATION OF DETECTING AE EVENTS ON THE PLATE BY A RESONANT CMUT

In this section, the ball drop impact test is simulated to verify the feasibility of detecting AE events on a plate by designed resonant CMUTs. The signal of the ball drop impact force is exerted on a point with the approximated expression given below:³¹

$$F(t) = \frac{2.28m_0gh}{\alpha} \sin\left(\frac{1.51\sqrt{gh}}{\alpha}(t - 50/f_0)\right), \quad (20)$$

$$50/f_0 \leq t \leq (50/f_0 + \pi\alpha/1.51\sqrt{gh}),$$

where

$$\alpha = \left(\frac{15\pi(\delta_0 + \delta_1)m_0gh}{8\sqrt{R_0}}\right)^{0.4},$$

$$\delta_0 = (1 - \nu_0)/(\pi E_0),$$

$$\delta_1 = (1 - \nu_1)/(\pi E_1).$$

In Eq. (20), m_0 is the mass of the ball, R_0 is the radius of the ball, ν_0 is Poisson's ratio of the ball, E_0 is Young's modulus of the ball, ν_1 is Poisson's ratio of the plate, E_1 is Young's modulus of the plate, g is the gravity acceleration, and h is the height of free fall.

In the simulation, the excitation time is at $t = 50/f_0$ (f_0 is the resonant frequency of CMUT II), the drop height is $h = 0.3$ m, the radius of the ball is $R_0 = 1.3$ mm, and the plate thickness is $d = 3$ mm. The materials of the ball and the plate are steel and aluminum, respectively. The designed cell of CMUT II is adopted to receive the AE signal of ball drop impact. The distance between the excitation point and the CMUT is set to 0.6 m. Figure 12 shows the simulated results of the ball drop impact. The impact force is exerted on the plate when time is 0.227 ms [Fig. 12(a)] (the maximal amplitude is about 66 N), with the spectra [Fig. 12(c)] covering a frequency range of about 0–400 kHz, where most of the frequencies are less than 180 kHz. The output current of CMUT is shown in Fig. 12(b), where the first arrived signal is at about

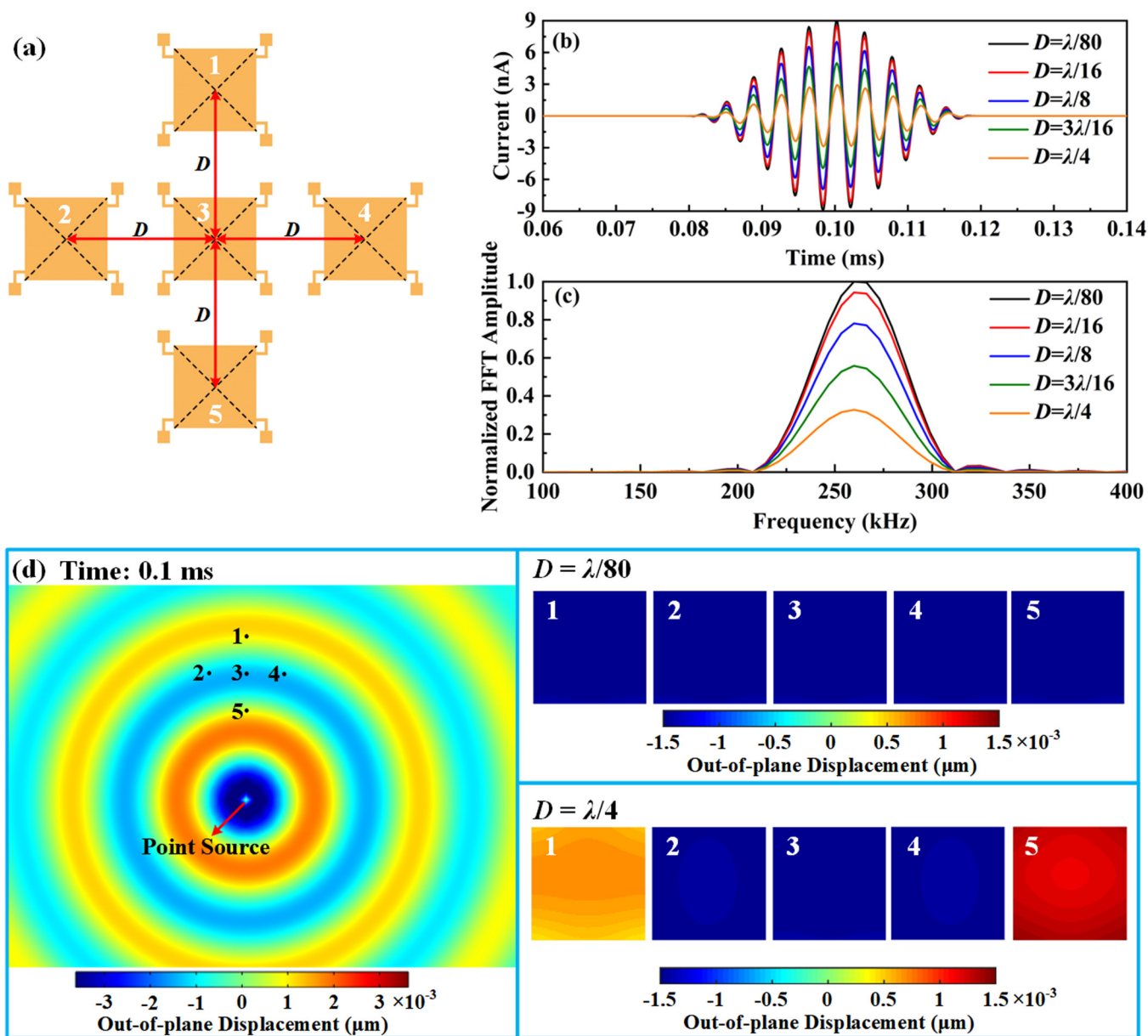


FIG. 11. Influence of the cell space D between CMUT cells on the total output currents, where the cells are arranged in a cross-like shape with $N=5$: (a) schematic diagram of the array; (b) the transient total output current with different cell spaces; (c) FFT results of (b), where the FFT amplitudes are normalized by dividing the FFT peak of $D = \lambda/80$. (d) The out-of-plane displacement distributions of the plate (left figure, the position of each CMUT cell is labeled by black spots) and the top electrode of each CMUT cell (right figure) at the time of 0.1 ms.

0.341 ms. According to dispersion curves given in Fig. 12(b), S0 lamb waves are fast and weak-dispersive in the low-frequency range (here, lower than 400 kHz), while the A0 lamb waves are slow and strong-dispersive. Thus, the first arrived signal is in the S0 mode, which can also be confirmed by out-of-plane displacement distributions of the plate around CMUT at 0.34 ms [Fig. 12(e)].

However, due to the short propagation distance, the arriving time of A0 lamb waves cannot be well determined. From the out-of-plane displacement distributions, the arrived signal at 0.4 ms is in the A0 mode [Fig. 12(f)]. Besides, FFT results of the current signal have shown that the CMUT can capture the signal with the frequency of around 220 kHz [see Fig. 12(d)]. Based on the

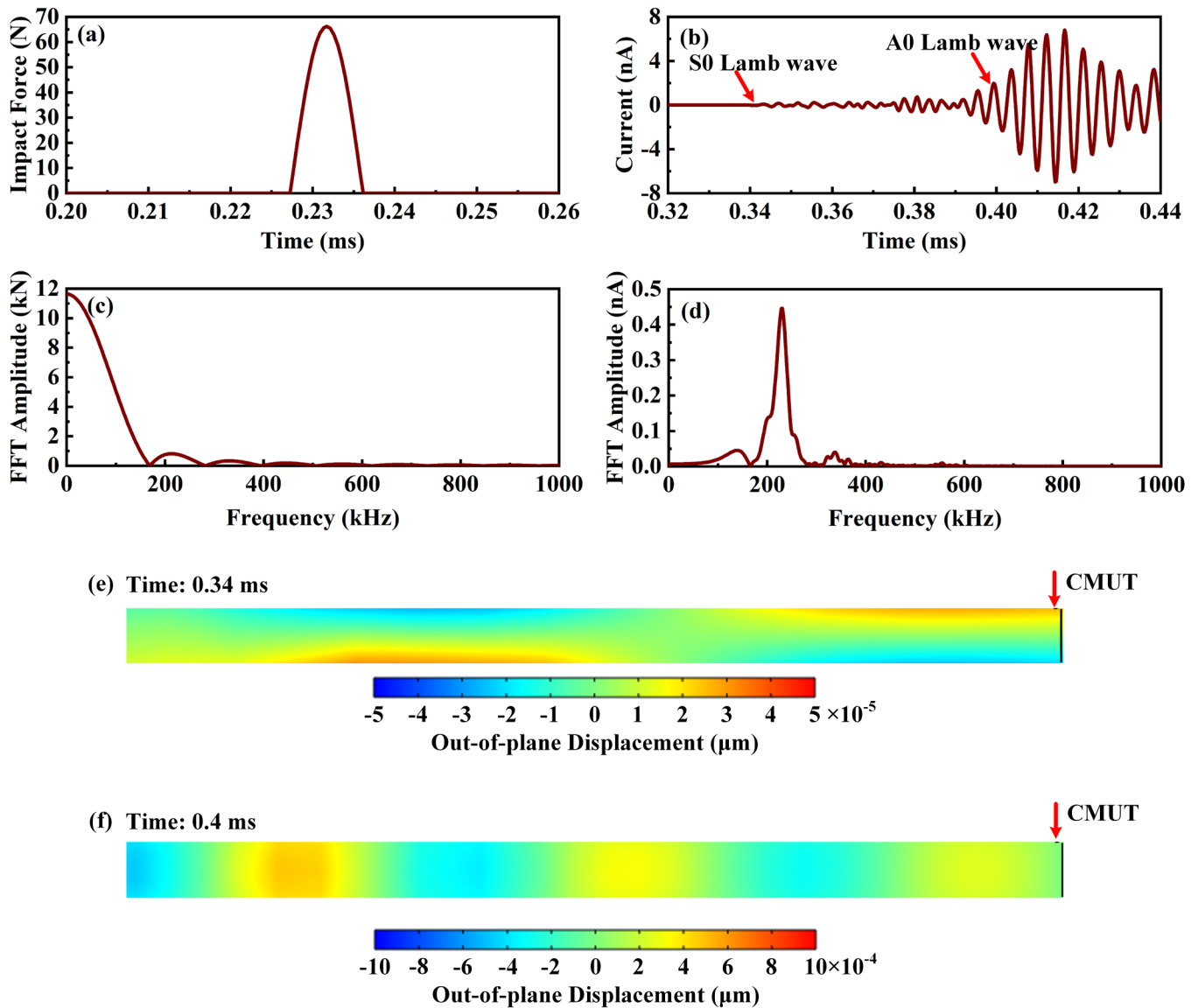


FIG. 12. (a) The time-domain signal of the ball drop impact; (b) the output current of CMUT; (c) FFT results of (a); (d) FFT results of (b); (e) the out-of-plane displacement distributions of the plate at 0.34 ms; and (f) the out-of-plane displacement distributions of the plate at 0.4 ms.

propagation distance and propagation time, the velocity of the S0 lamb wave is determined as 5275 m/s, which is almost equal to the theoretical result of group velocity at 220 kHz (5254 m/s). According to the propagation velocity of S0 and the time of arrival (TOA) of S0, we can determine a circle with the center of a CMUT as the origin. This circle is the position where the AE source may appear. Using three CMUTs, we can determine three circles. The intersection of these circles may be the location of the AE source. Besides TOA, there are many other locating theories, as shown in Ref. 32–34.

V. CONCLUSIONS

In this work, the feasibility of sensing the A0 and the S0 lamb waves using an out-of-plane sensitive resonant CMUT has been verified from the aspects of theory and FEM simulation. The results can be concluded as follows:

- (i) The designed CMUTs are sensitive to the out-of-plane displacements of Lamb waves and are extremely insensitive to the in-plane displacement of Lamb waves.

- (ii) Smaller squeezed-film damping may increase the output signal; however, it would produce a more serious tailing signal, which would lead to the superposition of signals. Therefore, the squeeze-film damping needs to be carefully designed to balance the output amplitude and tailing.
- (iii) For a small input signal, the output current of a resonant CMUT is linear. However, nonlinearity would become obvious when the amplitude of the input signal exceeds a threshold (for the CMUT designed in this work, the threshold is about 90 nm).
- (iv) The output current of a resonant CMUT is proportional to the number of its constituted cells when the span is far less than the incident wavelength. Besides, the phase would have little effect on the total output current when the cell span is less than $\lambda/8$.
- (v) According to the time of the first-arrived fast and weak-dispersive S0 Lamb waves, the location of the AE source may be feasible by using CMUTs. The location can be determined by some classical theory, e.g., time of arrival (TOA).

Our work has produced a way for predicting the sensing behaviors of CMUTs and is expected to promote the development of CMUTs in the field of Lamb wave-based AE detections. However, some deficiencies are existing in this work, e.g., the signal-to-noise ratios and the experimental investigation and experimental validation, which would be solved in our future work.

ACKNOWLEDGMENTS

This work was supported in part by the National Natural Science Foundation of China under Grant No. 62271235, the National Major Scientific Instrument Research Project of NSFC under Grant No. 61927807, the National Natural Science Foundation of China under Grant No. 62071205, and the Foundation of State Key Laboratory of Dynamic Testing Technology under Grant No. 2022-SYSJJ-10.

AUTHOR DECLARATIONS

Conflict of Interest

The authors have no conflict to disclose.

Author Contributions

Wei Lu: Formal analysis (lead); Methodology (lead); Writing – original draft (lead); Writing – review & editing (equal). **Sai Zhang:** Conceptualization (lead); Funding acquisition (equal); Supervision (lead). **Renxing Wang:** Writing – review & editing (equal). **Yuhua Yang:** Project administration (equal). **Guojun Zhang:** Writing – review & editing (equal). **Wendong Zhang:** Funding acquisition (equal); Supervision (equal). **Baiqiang Xu:** Funding acquisition (equal); Resources (lead); Software (lead). **Mehmet Yilmaz:** Supervision (equal); Writing – review & editing (equal).

DATA AVAILABILITY

The data that support the findings of this study are available from the corresponding author on reasonable request.

APPENDIX: DETAILED DERIVATIONS OF EQS. (9) AND (10)

Considering that Eq. (7) is a second-order non-homogeneous ordinary differential equation, its general solution should be expressed as the sum of a special solution to the equation and the general solution to the corresponding homogeneous equation.

First, Eq. (7) can be rewritten in the form of

$$\frac{d^2 Z}{dt^2} + 2\beta \frac{dZ}{dt} + \omega_0^2 Z = -\frac{d^2 Z_0}{dt^2}, \quad (\text{A1})$$

where

$$\beta = \frac{c}{2m}.$$

Then, the corresponding homogeneous equation of Eq. (A1) is

$$\frac{d^2 Z}{dt^2} + 2\beta \frac{dZ}{dt} + \omega_0^2 Z = 0, \quad (\text{A2})$$

where the characteristic equation of Eq. (A2) should be expressed as

$$r^2 + 2\beta r + \omega_0^2 = 0. \quad (\text{A3})$$

It is not difficult to find the roots of Eq. (A3) as

$$r_1 = -\beta + \sqrt{\beta^2 - \omega_0^2},$$

$$r_2 = -\beta - \sqrt{\beta^2 - \omega_0^2}.$$

Since the relationship between β and ω_0 is unknown, all cases may be discussed, as shown in the following:

- (i) If $\beta < \omega_0$ (under-damped), r_1 and r_2 should be a group of conjugate complex roots. The general solution to Eq. (A2) can be expressed as

$$Z(t) = e^{-\beta t} \left[C_1 \cos(\sqrt{\omega_0^2 - \beta^2} t) + C_2 \sin(\sqrt{\omega_0^2 - \beta^2} t) \right].$$

- (ii) If $\beta = \omega_0$ (critical damping), r_1 and r_2 should be equal real roots. The general solution to Eq. (A2) can be expressed as

$$Z(t) = e^{-\beta t} (C_1 + C_2 t).$$

- (iii) If $\beta > \omega_0$ (over-damped), r_1 and r_2 should be unequal real roots. The general solution of Eq. (A2) can be expressed as

$$Z(t) = C_1 e^{-\beta t + \sqrt{\beta^2 - \omega_0^2} t} + C_2 e^{-\beta t - \sqrt{\beta^2 - \omega_0^2} t},$$

where C_1 and C_2 can be determined by the initial conditions.

The special solution to Eq. (A1) should be assumed as

$$Z^*(t, \omega) = E_s e^{i\omega t}. \quad (\text{A4})$$

Substituting Eq. (A4) into Eq. (A1),

$$E_s = \frac{A\omega\omega^2}{\omega_0^2 - \omega^2 + 2i\omega\beta} = \frac{A\omega Q\omega^2}{Q(\omega_0^2 - \omega^2) + 2i\omega\beta Q} = \frac{A\omega Q\omega^2}{Q(\omega_0^2 - \omega^2) + i\omega\omega_0}. \quad (\text{A5})$$

Thus,

$$Z^*(t, \omega) = \frac{Q\omega^2}{Q(\omega_0^2 - \omega^2) + i\omega\omega_0} Z_0(t, \omega). \quad (\text{A6})$$

The general solution to Eq. (A1) should be the sum of $Z(t)$ and $Z^*(t, \omega)$, where the former describes the attenuated motion (if $t \rightarrow \infty$, $Z(t) \rightarrow 0$) of the “spring-mass-damping” system, and the latter describes the steady-state vibration of the system driven by an external force of angular frequency ω . Generally, the motion of a CMUT cell would be described just by the term $Z^*(t, \omega)$, since $Z(t)$ decays rapidly. Therefore, Eq. (A6) is the solution to Eq. (9).

The CMUT cell can be considered as a combination of parallel plate capacitors. If there is no DC bias voltage between the electrodes of a CMUT cell, the capacitance of the cell can be seen as the series connection of two parallel plate capacitors,

$$C = \frac{1}{\frac{1}{C_{Si_3N_4}} + \frac{1}{C_{gap}}} = \varepsilon_0 S \frac{1}{\frac{d_{Si_3N_4}}{\varepsilon_{Si_3N_4}} + d_{gap}} = \varepsilon_0 S \frac{1}{a}. \quad (\text{A7})$$

If a DC-biased voltage is applied between the electrodes of a CMUT cell, the top electrode would be pulled toward the bottom electrode by the electrostatic force. The displacement of the top electrode is described as $-d_0$. Thus, the corrected capacitance of a CMUT cell is given as

$$C = \varepsilon_0 S \frac{1}{a - d_0}. \quad (\text{A8})$$

According to Ref. 13, the electrostatic force applied on the top electrode can be approximated as

$$F_e = \frac{1}{2} V_{dc}^2 \frac{dC}{dd_0} = \frac{1}{2} V_{dc}^2 \varepsilon_0 S \left(\frac{1}{a^2} + \frac{2d_0}{a^3} \right). \quad (\text{A9})$$

At the same time, the tension of the effective spring would be applied on the top electrode,

$$F_s = kd_0. \quad (\text{A10})$$

Then, equating Eq. (A9) to Eq. (A10), the value of d_0 can be found as

$$d_0 = \frac{V_{dc}^2 \varepsilon_0 S a}{2(ka^3 - V_{dc}^2 \varepsilon_0 S)}. \quad (\text{A11})$$

REFERENCES

- O. Oralkan, A. S. Ergun, J. A. Johnson, M. Karaman, U. Demirci, K. Kaviani, T. H. Lee, and B. T. Khuri-Yakub, “Capacitive micro-machined ultrasonic transducers: Next-generation arrays for acoustic imaging,” *IEEE Trans. Ultrason. Ferroelectr. Freq. Control* **49**, 1596–1610 (2002).
- M. Vallet, F. Varray, J. Boutet, J.-M. Dinten, G. Caliano, A. S. Savoia, and D. Vray, “Quantitative comparison of PZT and CMUT probes for photoacoustic imaging: Experimental validation,” *Photoacoustics* **8**, 48–58 (2017).
- J. Johnson, Ö Oralkan, U. Demirci, S. Ergun, M. Karaman, and P. Khuri-Yakub, “Medical imaging using capacitive micro-machined ultrasonic transducer arrays,” *Ultrasonics* **40**, 471–476 (2002).
- Butterfly Network, see www.butterflynetwork.com/clinical/ob for information about CMUTs in medical ultrasound imaging (accessed on 11 January 2019).
- Y. Pei, Y. Zhang, S. M. Hu, Z. H. Wang, Y. F. Li, C. D. He, S. Zhang, R. X. Wang, W. D. Zhang, and G. J. Zhang, “Breast Transmission Ultrasound Tomography Based on Capacitive Micromachined Ultrasonic Transducer Linear Arrays,” *IEEE Sens. J.* **22**, 1209–1217 (2022).
- Y. Pei, G. Zhang, S. Zhang, Y. Zhang, T. Zhang, Z. Wang, and W. Zhang, “3D cone-beam breast ultrasonic tomography imaging for capacitive micromachined ultrasonic transducer cylindrical array,” *JASA Express Lett.* **1**, 022001 (2021).
- S. H. Wong, M. Kupnik, R. D. Watkins, K. Butts-Pauly, and B. T. Khuri-Yakub, “Capacitive micromachined ultrasonic transducers for therapeutic ultrasound applications,” *IEEE Trans. Biomed. Eng.* **57**, 114–123 (2010).
- J. W. Choe, O. Oralkan, A. Nikoozadeh, M. Gencel, D. N. Stephens, M. O’Donnell, D. J. Sahn, and B. T. Khuri-Yakub, “Volumetric real-time imaging using a CMUT ring array,” *IEEE Trans. Ultrason. Ferroelectr. Freq. Control* **59**, 1201–1211 (2012).
- F. L. Degertekin, R. O. Guldiken, and M. Karaman, “Annular-ring CMUT arrays for forward-looking IVUS: Transducer characterization and imaging,” *IEEE Trans. Ultrason. Ferroelectr. Freq. Control* **53**, 474–482 (2006).
- D. Ozevin, S. P. Pessiki, D. W. Greve, and I. J. Oppenheim, “Adapting a CMUT transducer to detect acoustic emissions,” in *Proceedings of IEEE Ultrasonics Symposium* (IEEE, 2005), pp. 956–959.
- A. P. Wright, W. Wu, I. J. Oppenheim, and D. W. Greve, “Damping, noise, and in-plane response of MEMS acoustic emission sensors,” *J. Acoust. Emiss.* **25**, 115–123 (2007).
- C. Auerswald, A. Sorger, M. Diemel, A. Shaporin, and J. Mehner, “MEMS acoustic emission sensor with mechanical noise rejection,” in *International Multi-Conference on Systems, Signals and Devices* (IEEE, 2012), pp. 1–6.
- H. Saboonchi and D. Ozevin, “MEMS acoustic emission transducers designed with high aspect ratio geometry,” *Smart Mater. Struct.* **22**, 095006 (2013).
- M. Kabir, H. Saboonchi, and D. Ozevin, “The design, characterization, and comparison of MEMS comb-drive acoustic emission transducers with the principles of area-change and gap-change,” in *Proceedings of SPIE—The International Society for Optical Engineering* (SPIE, 2015), pp. 698–709.
- H. Saboonchi, D. Ozevin, and M. Kabir, “MEMS sensor fusion: Acoustic emission and strain,” *Sens. Actuat. A: Phys.* **247**, 566–578 (2016).
- W. Lu, S. Zhang, R. X. Wang, B. Q. Xu, M. Yilmaz, and W. D. Zhang, “Theoretical and simulation studies on designing a phase-reversal-based broadband CMUT with flat passband and improved noise rejections for SHM,” *IEEE Sens. J.* **22**, 3210292 (2022), in publication, doi:10.1109/JSEN.2022.
- T. M. Roberts and M. Talebzadeh, “Acoustic emission monitoring of fatigue crack propagation,” *J. Constr. Steel Res.* **59**, 695–712 (2003).
- M. Fotouhi and M. A. Najafabadi, “Acoustic emission-based study to characterize the initiation of delamination in composite materials,” *J. Thermoplast. Compos. Mater.* **29**, 519–537 (2016).
- D. G. Aggelis, E. Z. Kordatos, and T. E. Matikas, “Acoustic emission for fatigue damage characterization in metal plates,” *Mech. Res. Commun.* **38**, 106–110 (2011).
- G. Gautschi, *Piezoelectric Sensorics* (Springer-Verlag, 2001).

- ²¹W. J. Staszewski, B. C. Lee, and R. Traynor, "Fatigue crack detection in metallic structures with lamb waves and 3D laser vibrometry," *Meas. Sci. Technol.* **18**, 727–739 (2007).
- ²²P. Aryan, A. Kotousov, C. T. Ng, and B. S. Cazzolato, "A baseline-free and non-contact method for detection and imaging of structural damage using 3D laser vibrometry," *Struct. Control Health Monitoring* **24**, e1894 (2017).
- ²³D. W. Greve, I. J. Oppenheim, W. Wu, and A. P. Wright, "Development of a MEMS acoustic emission sensor system," in *Sensors and Smart Structures Technologies for Civil, Mechanical, and Aerospace Systems* (SPIE, 2007).
- ²⁴R. Boubenia, G. Bourbon, P. Le Moal, E. Joseph, E. Ramasso, and V. Placet, "Acoustic emission sensing using MEMS for structural health monitoring: Demonstration of a newly designed capacitive micro-machined ultrasonic transducer," in *12th International Workshop on Structural Health Monitoring* (Stanford, CA, 2019).
- ²⁵R. Boubenia, P. Le Moal, G. Bourbon, E. Ramasso, and E. Joseph, "CMUT-based sensor for acoustic emission application: Experimental and theoretical contributions to sensitivity optimization," *Sensors* **21**, 2042 (2021).
- ²⁶Z. Su and L. Ye, *Identification of Damage Using Lamb Waves: From Fundamentals to Applications* (Springer Science & Business Media, 2009).
- ²⁷J. L. Rose, *Ultrasonic Guided Waves in Solid Media* (Cambridge University Press, 2014).
- ²⁸A. W. Harris, I. J. Oppenheim, and D. W. Greve, "MEMS-based high-frequency vibration sensors," *Smart Mater. Struct.* **20**, 075018 (2011).
- ²⁹D. Ozevin, D. W. Greve, I. J. Oppenheim, and S. P. Pessiki, "Resonant capacitive MEMS acoustic emission transducers," *Smart Mater. Struct.* **15**, 1863–1871 (2006).
- ³⁰A. P. Wright, D. W. Greve, and I. J. Oppenheim, "Sensitivity of a MEMS acoustic emission sensor system," in *Sensors and Smart Structures Technologies for Civil, Mechanical, and Aerospace Systems* (SPIE, 2009), pp. 72920R–72920R-9.
- ³¹W. Goldsmith, *Impact: The Theory and Physical Behavior of Colliding Solids* (Dover, New York, 2001).
- ³²D. Aljets, A. Chong, S. Wilcox, and K. Holford, "Acoustic emission source location on large plate-like structures using a local triangular sensor array," *Mech. Syst. Signal Process.* **30**, 91–102 (2012).
- ³³A. Tobias, "Acoustic-emission source location in two dimensions by an array of three sensors," *Non-Destruct. Testing* **9**, 9–12 (1976).
- ³⁴M. G. Baxter, R. Pullin, K. M. Holford, and S. L. Evans, "Delta T source location for acoustic emission," *Mech. Syst. Signal Process.* **21**, 1512–1520 (2007).